Competition between static and dynamic magnetism in the Kitaev spin liquid material Cu_2IrO_3

Eric M. Kenney[1], Carlo U. Segre[2], William Lafargue-Dit-Hauret[3], Oleg I. Lebedev[4], Mykola Abramchuk[1], Adam Berlie[5], Stephen P. Cottrell[5], Gediminas Simutis[6], Faranak Bahrami[1], Natalia E. Mordvinova[4], Jessica. L. McChesney[7], Gilberto Fabbris[7], Daniel Haskel[7], Xavier Rocquefelte[3], Michael J. Graf[1], & Fazel Tafti[1]

[1]*Department of Physics, Boston College, Chestnut Hill, MA 02467, USA*

[2]*Department of Physics & CSRRI, Illinois Institute of Technology, Chicago, IL 60616, USA*

[3]*Univ Rennes, ENSCR, CNRS, ISCR (Institut des Sciences Chimiques de Rennes) - UMR 6226, F-35000 Rennes, France*

[4]*Laboratoire CRISMAT, ENSICAEN-CNRS UMR6508, 14050 Caen, France*

[5]*ISIS Neutron and Muon Source, Science and Technology Facilities Council, Rutherford Appleton Laboratory, Didcot, OX11 0QX, United Kingdom*

[6]*Laboratory for Muon Spin Spectroscopy, Paul Scherrer Institute, 5232 Villigen PSI, Switzerland*

[7]*Advanced Photon Source, Argonne National Laboratory, Argonne IL 60439, USA*

arXiv:1811.00565v1 [cond-mat.str-el] 1 Nov 2018

Anyonic excitations emerging from a Kitaev spin liquid can form a basis for quantum computers [1,2]. Searching for such excitations motivated intense research on the honeycomb iridate materials [3–17]. However, access to a spin liquid ground state has been hindered by magnetic ordering [5]. Cu_2IrO_3 is a new honeycomb iridate without thermodynamic signatures of a long-range order [18]. Here, we use muon spin relaxation to uncover the magnetic ground state of Cu_2IrO_3. We find a two-component depolarization with slow and fast relaxation rates corresponding to distinct regions with dynamic and static magnetism, respectively. X-ray absorption spectroscopy and first principles calculations identify a mixed copper valence as the origin of this behavior. Our results suggest that a minority of Cu^{2+} ions nucleate regions of static magnetism whereas the majority of Cu^{+}/Ir^{4+} on the honeycomb lattice give rise to a Kitaev spin liquid.

Long-range magnetic order is the natural ground state of an interacting electron system. Magnetic frustration is capable of disrupting the order and establishing a highly entangled ground state with non-local excitations known as a quantum spin liquid [19]. Among various spin liquid proposals, the Kitaev model has unique appeal because it offers an exact solution to a simple Hamiltonian $\left(H_{ij} = -\sum_{\gamma} K_{\gamma} S_i^{\gamma} S_j^{\gamma}\right)$ of spin-$1/2$ particles with bond dependent ferromagnetic coupling (K_{γ}) [1]. The index γ corresponds to three inequivalent bonds at 120° on a honeycomb lattice. Two alkali iridates, Li_2IrO_3 and Na_2IrO_3, were the first proposed Kitaev materials based on their honeycomb lattice structures that accommodate Ir^{4+} ions with pseudospin-1/2 ($J_{\text{eff}} = 1/2$) [3–5,20–22]. Despite satisfying the basic assumptions of a Kitaev model, both compounds exhibited antiferromagnetic ordering with sharp peaks in both DC-magnetization and heat capacity at 15 K [4,9]. Further investigations on the honeycomb [13,14], hyperhoneycomb [15,16], and harmonic honeycomb [17] materials revealed the presence of a Heisenberg interaction (J) and a symmetric off-diagonal interaction (Γ) in the modified Hamiltonian of Kitaev materials [23,24]:

$$\mathcal{H} = \sum_{<i,j>,\gamma\neq\alpha,\beta} \left[-K_{\gamma} S_i^{\gamma} S_j^{\gamma} + J\mathbf{S}_i \cdot \mathbf{S}_j + \Gamma\left(S_i^{\alpha} S_i^{\beta} + S_i^{\beta} S_i^{\alpha}\right)\right] \tag{1}$$

The search for a Kitaev material with a negligible Heisenberg interaction and without a long-range order has recently lead to a new honeycomb copper iridate, Cu_2IrO_3 [18]. Despite having a similar magnetic moment and Curie-Weiss temperature as the alkali iridates, Cu_2IrO_3 barely revealed a small peak in DC-magnetization at 2 K and a broad hump in the heat capacity [18]. These results indicated short-range correlations and suggested proximity to the Kitaev spin liquid phase. A spin liquid ground state is expected to exhibit dynamical local fields without long-range ordering. In this letter, we use muon spin relaxation (μSR) as a direct probe of local magnetic fields and provide

compelling evidence for a Kitaev spin liquid phase in Cu_2IrO_3. Furthermore, our μSR results reveal a competition between dynamic and static magnetism in distinct volumes in the ground state. The source of such behavior is traced to a mixed valence of Cu^{+}/Cu^{2+} by X-ray absorption spectroscopy and first-principles calculations.

In μSR, spin polarized positive muons are implanted in the sample, and the time evolution of the muon spin polarization in the local magnetic field is traced upon accumulating several million muon decay events. In Fig 1a, we show three muon polarization spectra in zero applied field (ZF) at 16, 4.5, and 0.05 K, and one spectrum at 16 K in a 50 Oe applied field parallel to the initial muon polarization (longitudinal field, or LF). The ZF spectra at all temperatures are described by

$$P(t) = G_{KT}(t)\left[(1-f)\exp(-\lambda_{\text{slow}}t) + f\exp(-\lambda_{\text{fast}}t)\right] \quad (2)$$

where $G_{KT}(t)$ is the Gaussian Kubo-Toyabe function describing depolarization by quasi-static randomly oriented magnetic moments [25] according to $G_{\text{KT}}(t) = \frac{1}{3} + \frac{2}{3}(1-\Delta^2t^2)\exp(-\frac{1}{2}\Delta^2t^2)$. Fits at 16 K yield $\Delta = 0.11$ μs^{-1}, a typical rate for depolarization by nuclear moments [26]. As expected, this relaxation channel is largely suppressed by a weak LF of 50 Oe (Fig. 1a). The slow and fast exponential decays (λ_{slow} and λ_{fast}) represent a two-component electronic spin contribution to the muon depolarization, and f is the fraction of the signal associated with the fast decay. We will show below that λ_{slow} and λ_{fast} correspond to muons depolarizing in regions of dynamic and static magnetism, respectively.

In Fig. 1a, the fast relaxation is primarily observed as a missing polarization at $t < 0.2$ μs which is outside the bandwidth of the pulsed muon facility. However, enough of the fast relaxation

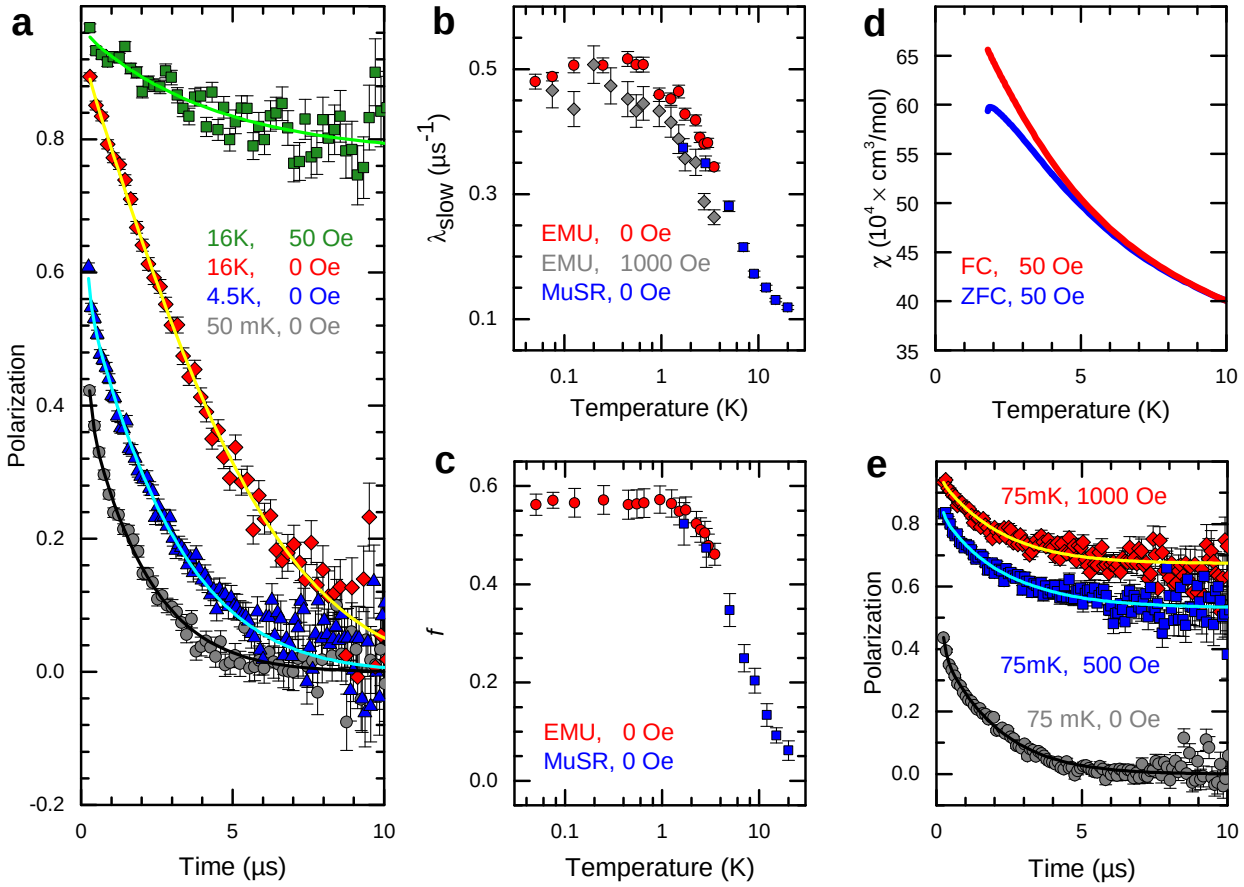


Figure 1: | μ**SR data.** **a,** Representative zero field (ZF) spectra obtained at 16 K (red diamonds), 4.5 K (blue triangles), and 0.05 K (gray circles) as well as longitudinal field (LF) spectrum at 16 K and 50 Oe (green squares). Continuous lines are fits to the data. Supplementary μSR data are presented in Fig. S1. **b,** Temperature dependence of the slow depolarization rate λ_{slow} shows a plateau below 2 K at both ZF and LF of 1000 Oe with data extending over two decades of temperature from 20 to 0.05 K. **c,** Temperature dependence of the fast depolarization fraction f shows a plateau below 2 K. **d,** DC magnetic susceptibility shows a small peak at 2 K and a splitting between field-cooled (FC) and zero-field-cooled (ZFC) at 10 K. **e,** μSR spectra at 75 mK in several longitudinal fields show a persistent slow depolarization and a vanishing fast depolarization component.

tail leaks into the spectra in Fig. 1a to fit its contribution with a temperature independent relaxation rate $\lambda_{\text{fast}} = 9(3)\ \mu\text{s}^{-1}$. A pulsed muon source is particularly suitable to characterize the slow mode with relaxtion rate $\lambda_{\text{slow}} = 0.48(1)\ \mu\text{s}^{-1}$at 50 mK (Fig. 1b) which is 18 times slower than λ_{fast}. Temperature dependences of λ_{slow} and f are shown in Fig. 1b,c. The slow and fast modes grow rapidly below 10 K. This onset of magnetism correlates with the temperature at which the field-cooled (FC) and zero-field-cooled (ZFC) susceptibility curves deviate (Fig. 1d). With further decreasing temperature, both λ_{slow} and f form plateaus below $T = 2$ K (Fig. 1b,c). The onset of a plateau in f coincides with a small peak in the ZFC susceptibility (Fig. 1d), suggesting the presence of frozen spins in a fraction of the sample volume.

Field dependence of μSR can be used to probe the dynamics of the slow and fast modes. Figure 1e shows that the application of a 1000 Oe LF restores the missing polarization from the fast relaxing muons, indicating the fast relaxation is caused by static local fields that are significantly less than 1000 Oe. In contrast, relaxation of the slow component appears to be due to dynamic rather than static local fields. Because $\lambda_{\text{slow}} \ll \lambda_{\text{fast}}$, if the local fields were static for slow relaxing muons, we would expect the slow channel to also be suppressed by the 1000 Oe LF. Indeed, if the slow relaxation were caused by a static field, the magnitude of that field would be approximated by $B_i = 2\pi\lambda_{\text{slow}}/\gamma_\mu = 37$ Oe $\ll 1000$ Oe ($\gamma_\mu/2\pi = 135.5$ MHzT^{-1} is the muon gyromagnetic ratio). The nearly unchanged relaxation rate and amplitude of the slow mode in 1000 Oe LF (Fig. 1b,e) demonstrate that it is caused by fluctuating local fields. Therefore, we ascribe λ_{fast} to muons depolarizing in static magnetic domains, and λ_{slow} to muons depolarizing in distinct regions with spin-liquid-like fluctuating local fields. The observation of a slight decrease

in amplitude of the slow depolarization in Fig. 1e, in contrast to the nearly complete suppression of the fast mode suggests that dynamic and static magnetism do not coexist, but rather compete with one another. The dynamic component is consistent with theoretical predictions of a Kitaev spin liquid in honeycomb iridates [11,21,23,27] but the source of static magnetism is unclear. Next, we use spectroscopic techniques to clarify this.

Charge neutrality in Cu_2IrO_3 dictates conjugate oxidation states of either Cu^+ and Ir^{4+}, or Cu^+/Cu^{2+} and Ir^{3+}. Cu^+ $[3d^{10}]$ is nonmagnetic whereas Cu^{2+} $[3d^9]$ is magnetic with $S = 1/2$. Ir^{3+} $[5d^6]$ is nonmagnetic whereas Ir^{4+} $[5d^5]$ is magnetic with $J_{\text{eff}} = 1/2$ due to one hole in the t_{2g} level [28]. Each unit cell of Cu_2IrO_3 (Fig. 2a) contains three copper sites between the layers (Cu2,3,4) in a dumbbell coordination and one copper site (Cu1) within the honeycomb layers in an octahedral coordination [18]. The typical coordination for Cu^+ is linear (dumbbells) and for Cu^{2+} is square planar. An octahedral environment can accommodate both Cu^+ and Cu^{2+}. Based on this argument we expect at least 75% of Cu^+ in Cu_2IrO_3.

X-ray absorption near edge spectroscopy (XANES) is a powerful tool to probe oxidation states. Our XANES data in Fig 2b show identical normalized absorption coefficients $\mu(E)$ for Cu K-edge at 300 and 85 K confirming a temperature independent ratio Cu^+/Cu^{2+} (see Fig. S2 for Ir L_3-edge). Figure 2c compares the Cu K-edge in Cu_2IrO_3 at room temperature to Cu, CuO, and Cu_2O. The close similarity with Cu_2O indicates a majority of Cu^+. We calculated $\mu(E)$ for the individual sites, Cu1 to Cu4, using the FEFF 8.40 code [29] based on the crystallographic data. The results in Fig. 2d show that Cu1 has a spectrum different from Cu2,3,4 as expected from the

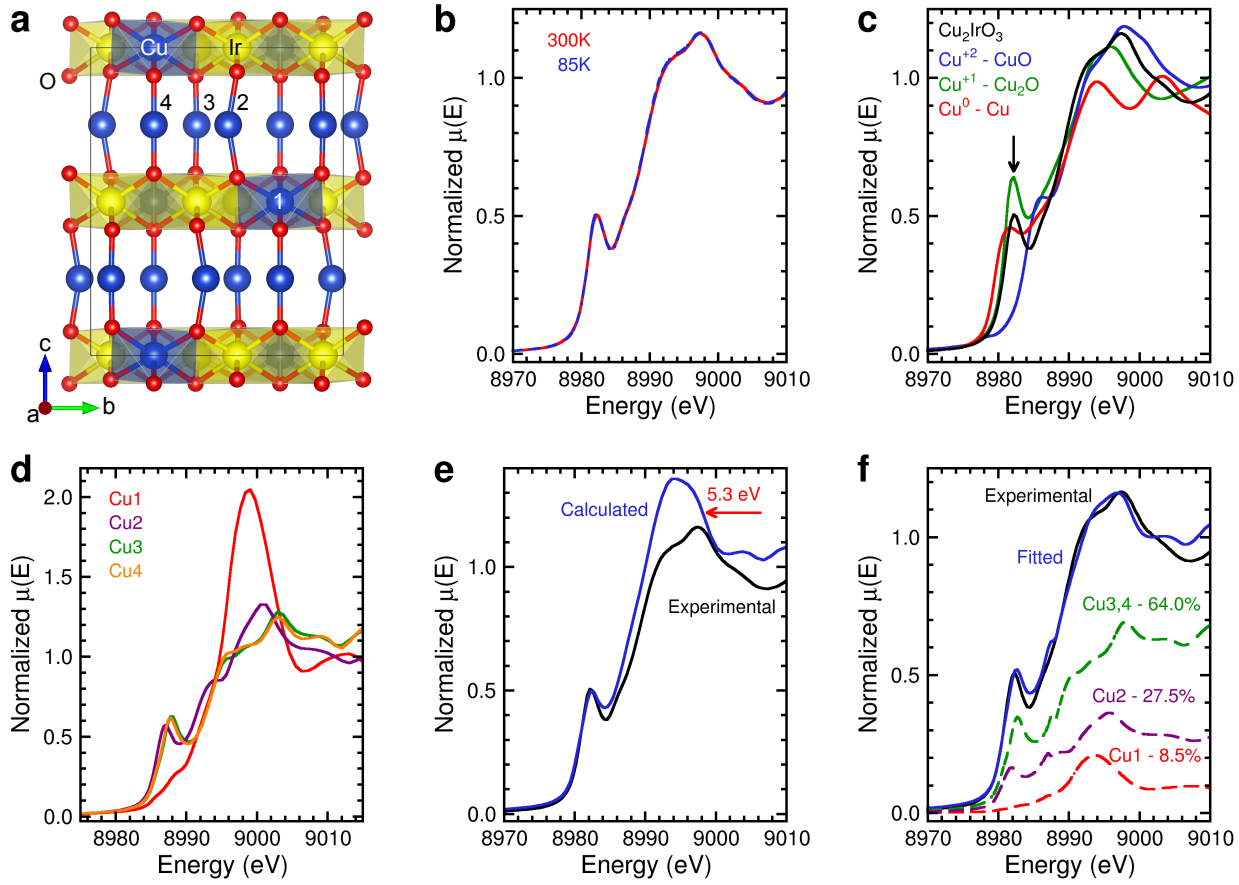


Figure 2: | **XANES data.** **a,** A Unit cell of Cu_2IrO_3 viewed down the a–axis with four distinct copper sites. Cu1 in octahedral coordination is within the honeycomb layers whereas Cu2, Cu3, and Cu4 in dumbbell coordination are between the layers. **b,** Normalized absorption coefficient plotted as a function of energy in Cu_2IrO_3. $\mu(E)$ curves are identical at 85 and 300 K. **c,** Comparing $\mu(E)$ between Cu_2IrO_3 and three standard references. **d,** Calculated absorption edge of Cu1 to Cu4 using the FEFF software. **e,** Absorption spectrum of Cu K-edge is calculated by summing over the partial contributions from Cu1 to Cu4 with equal weights. The calculated signal is shifted by 5.3 eV to match the experimental data with acceptable but not perfect agreement. **f,** A fit is made to the experimental XANES data where the weight of each partial contributions is a free parameter. The resulting weights for Cu1 to Cu4 are reported. Cu3 and Cu4 have the same weight.

coordination environments. Specifically, the edge for Cu1 is shifted to higher energy than the others, indicating a probable Cu^{2+} state. Since all copper sites in Cu_2IrO_3 have the same Wyckoff multiplicity [18], it is conceivable to reproduce the experimental curve by adding the four partial contributions in Fig. 2d with equal weight (25%). The resulting curve in Fig. 2e shows a mild disagreement with the experimental data. Specifically, the contribution from Cu1 (nominally Cu^{2+}) appears to be overestimated. The experimental data can be more precisely fit to a weighted sum of partial $\mu(E)$ contributions as reported on Fig. 2f. According to this analysis, we estimate 8.5% Cu^{2+} content which means the honeycomb layers contain $1/3$ Cu^{2+} $\left(\frac{8.5\%}{25\%}\right)$ and $2/3$ Cu^{+}. This is only a rough estimate because we do not know the detailed structure of $\mu(E)$ for Cu^{+} in octahedral coordination. Analysis of XANES data from Cu $L_{2,3}$-edges in the Supplementary Fig. S3 yields an average Cu^{2+} content of 13% which means the honeycomb layers contain $1/2$ Cu^{2+} $\left(\frac{13\%}{25\%}\right)$ and $1/2$ Cu^{+}. These results are substantiated by self-consistent DFT calculations in the Supplementary Fig. S4 where the spectroscopic data are best reproduced using 12% Cu^{2+} content. The spin-1/2 Cu^{2+} ions can nucleate regions of static magnetism within each honeycomb layer giving rise to a fast depolarization of muons (λ_{fast}). Outside these regions, the Cu^{+}/Ir^{4+} combination gives rise to a spin liquid phase with dynamical local fields giving rise to a slow depolarization of muons (λ_{slow}).

The most fundamental ingredient of a Kitaev material, apart from having spin-$1/2$ ions, is the honeycomb geometry. A direct image of Cu_2IrO_3 lattice is presented in Fig. 3a obtained by transmission electron microscopy (TEM). The middle panel is a high angle annular dark field scanning TEM image (HAADF-STEM) viewing down the $[100]$ axis of a small crystallite. It reveals

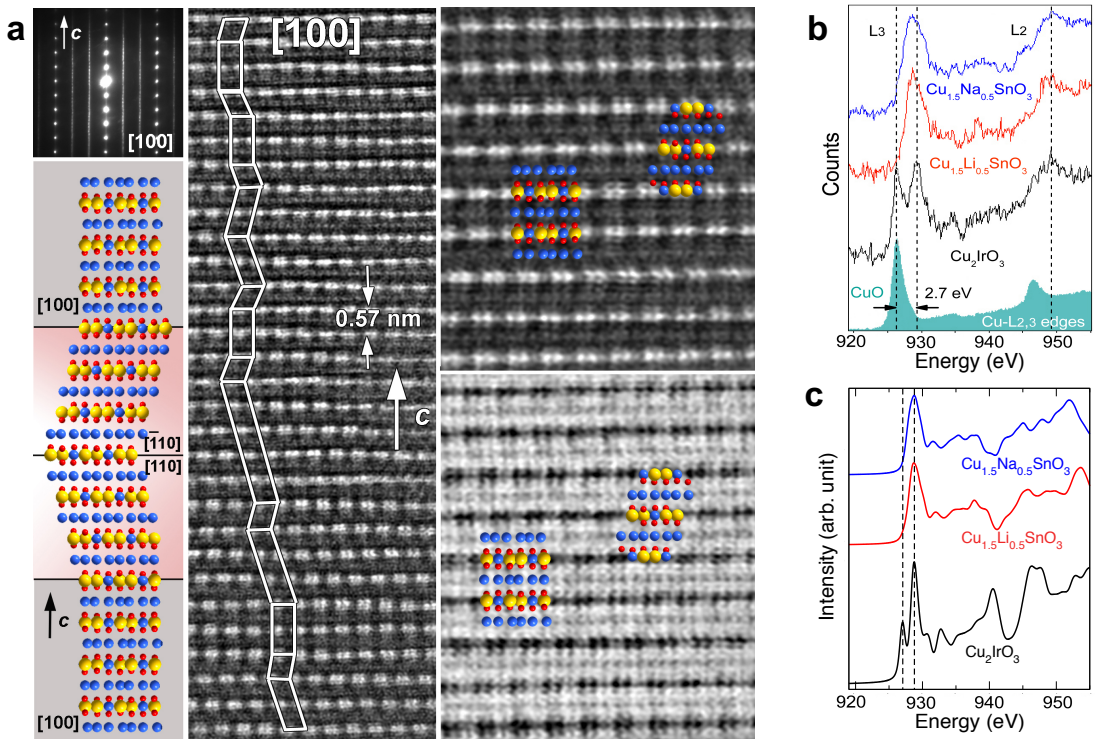


Figure 3: | **TEM and EELS data.** **a,** Scanning transmission electron microscopy (STEM) is used to reveal perfect honeycomb ordering and twinned stacking disorder in Cu_2IrO_3. Top left image is an electron diffraction pattern along $[100]$ where the streaking reveals stacking disorder along c-axis. Middle panel shows HAADF-STEM image along $[100]$ with a zigzag stacking that is modeled in the left inset as a twinning between $[100]$, $[110]$, and $[\bar{1}10]$ directions. Yellow, blue, and red circles represent Ir, Cu, and O atoms, respectively. Right top and bottom panels are magnified HAADF-STEM and ABF-STEM images, respectively. **b,** Experimental EELS spectra are compared between the stannates, $Cu_{1.5}Li_{0.5}SnO_3$ and $Cu_{1.5}Na_{0.5}SnO_3$, and the iridate Cu_2IrO_3. Only one L_3 peak is observed in the stannates corresponding to Cu^+ (note the CuO reference). Cu_2IrO_3 shows two L_3 peaks corresponding to Cu^+ and Cu^{2+}. **c,** Self-consistent DFT calculations reproduce EELS spectra in agreement with the experiments. The calculations reveal one peak in stannates corresponding to Cu^+ in dumbbell coordination but two peaks in Cu_2IrO_3 due to mixed valence of copper (see Supplementary information for details of DFT calculations).

a zigzag stacking pattern along the c-axis that is modeled in the left inset as a rotation (twinning) between adjacent layers with alternating $[100]$, $[110]$, and $[\bar{1}10]$ orientations. A similar twinned stacking disorder, i.e. $\pm 60^\circ$ rotation between adjacent layers, is observed in related stannate materials, $Cu_{1.5}Li_{0.5}SnO_3$ and $Cu_{1.5}Na_{0.5}SnO_3$ with alkali/tin honeycomb layers [30]. In the right upper and lower insets of Fig. 3a, unit cell models with $[100]$ and $[\bar{1}10]$ orientations are overlaid on magnified views of the HAADF-STEM and ABF-STEM (annular bright field scanning TEM) images, respectively. In both images, the layers exhibit a flawless pattern of Ir pairs separated by individual Cu atoms which is characteristic of honeycomb ordering [30]. Therefore, despite a twinned stacking disorder, each individual layer in Cu_2IrO_3 has perfect honeycomb ordering without site mixing or vacancies.

TEM is also used for electron energy loss spectroscopy (EELS) with the data presented in Fig. 3b. A comparison between the L_3-edge in stannates and Cu_2IrO_3 confirms that Cu_2IrO_3 contains both Cu^+ and Cu^{2+} whereas the stannates contain only Cu^+. In the stannate materials, Cu atoms are restricted between the honeycomb layers in a dumbbell coordination [30]. Thus, all Cu^{2+} in Cu_2IrO_3 must be contained within the layers. Self-consistent DFT calculations in Fig. 3c reproduce the EELS spectra and confirm a single L_3 peak in stannates but two distinct peaks in Cu_2IrO_3.

The emerging picture from our experimental and theoretical results is as follows. Cu_2IrO_3 contains a majority/minority of Cu^+/Cu^{2+}. The minority Cu^{2+} comprises about $1/3$ to $1/2$ of the copper ions within the honeycomb layers and nucleate regions of static magnetism with short-

range correlations. The majority of Cu^{+} ions render a majority of Ir^{4+} ions with $J_{\text{eff}} = 1/2$ within the layers forming regions of Kitaev spin liquid phase. Muons could implant either in the static magnetic domains and exhibit fast depolarization or in the spin liquid domains and exhibit slow depolarization. The competition between static and dynamic magnetism revealed by μSR highlights the robustness of the spin liquid phase in Cu_2IrO_3 and its ability to compete with static magnetism on equal footing.

Methods

Material Synthesis. Cu_2IrO_3 was synthesized using a topotactic cation exchange reaction according to Na_2IrO_3 + 2CuCl $\rightarrow$ Cu_2IrO_3 + 2NaCl under mild conditions (350 °C and 16 h). Details of the synthesis are explained in reference [18].

Muon Spin Relaxation. μSR measurements were performed at the ISIS Pulsed Neutron and Muon Source at the Rutherford Appleton Laboratories (UK) using the EMU and MuSR spectrometers with the sample inside a dilution refrigerator and a helium exchange cryostat, respectively. The powder sample was pressed into a disk of 8 mm diameter and 1.9 mm thickness, and was wrapped in a 12.5 μm thin silver foil. Measurements in EMU were performed on a silver mounting pedestal in a Dilution fridge (50 mK$< T <$4.5 K, along with data at 16.4 K). Due to the small sample area, measurements inside the dilution refrigerator were made in flypast mode (SI reference) in order to reduce the signal from muons not landing in the sample. In this case, the background results from muons landing in the cryostat. Measurements in the MuSR spectrometer were performed with the same sample mounted on a silver mounting plate in a helium exchange cryostat (1.7 K$< T <$ 20 K). In this case the background results from muons landing in the silver holder. The background signals for each spectrometer were fixed at the values determined from long-time asymmetry at low temperatures (40% of the total signal for EMU, 76% for MuSR), where the sample was strongly magnetic. The total asymmetry was fixed at the value determined from the initial asymmetry at high temperatures where the material had no fast relaxing component. The sample contribution to the asymmetry is the difference between these two values. Data were fit using WIMDA software (SI reference) and all fits had a χ^2 per degree of freedom of approximately

1.01. The fitting parameter α, which quantifies the efficiency mismatch between front and back detectors [25], was determined by the application of a weak transverse magnetic field.

X-ray absorption near edge spectroscopy (XANES) XANES measurements were performed at the Materials Research Collaborative Access Team (MRCAT), Sector 10-BM beam line at Argonne National Laboratory's Advanced Photon Source. Between 2 and 5 mg of A_2IrO_3 (A = Li, Na, Cu) as well as IrO_2 powders were thoroughly ground with BN as a filler and PVDF (polyvinylidene fluoride) as a binder, pressed into a 5 mm diameter pellet, and encapsulated in thin Kapton tape. Low temperature measurements were taken in transmission mode using a liquid nitrogen cooled stage (Linkam Scientific) at the Ir L_3-edge and the Cu K-edge. The XANES data were reduced using the Athena program and fitted to structural models using the Artemis program, both of the IFEFFIT suite (SI reference). Ir data were fitted with a single Ir–O path using a range of 2–12 Å^{-1} ($dk = 4$ Å^{-1}) in k-space and 1–2 Å ($dR = 0.2$ Å) in R-space and a weighting factor of k^2. Cu data were fitted using the same ranges but with multiple weighting factors of k, k^2, and k^3 [29]. Cu data were fitted with a single Cu–O path as well as multiple Cu–O paths. Cu L-edge data were collected at room temperature in total electron yield mode at the IEX beamline, 29-ID of the Advanced Photon Source, Argonne National Laboratory. The beamline resolution was 250 meV.

Electron Microscopy. Transmission electron microscopy (TEM) including electron diffraction (ED) and high angle annular dark field scanning TEM (HAADF–STEM), annular bright field scanning TEM (ABF–STEM), and electron energy loss spectroscopy (EELS) experiments were performed using an aberration double–corrected JEM ARM200F microscope operated at 200 kV and equipped with a CENTURIO EDX detector, Orius Gatan CCD camera and GIF Quantum spec-

trometer. TEM samples were prepared by grinding the materials in an agate mortar with ethanol and depositing the obtained suspension on a Ni–carbon holey grid.

Density Functional Theory. The geometric optimization of Cu_2IrO_3, $Cu_{1.5}Na_{0.5}SnO_3$, and $Cu_{1.5}Li_{0.5}SnO_3$ were implemented in the pseudopotential VASP code (SI reference) using a projected augmented wave (PAW) method and the Perdew-Burke-Ernzerhof (PBE) exchange-correlation potential (SI reference). The Hubbard correction was implemented using the Dudarev's scheme (SI reference) with $U_{\text{eff}} = 3$ eV for iridium $5d$ orbitals and 5 eV for copper $3d$ orbitals. The atomic positions were relaxed until forces were converged to 0.03 eV/Å. Simulations of the spectroscopic data were implemented in the full potential Wien2k code (SI reference) using a linearized augmented plane wave (LAPW) approach and PBE0 hybrid functional with on-site corrections to iridium $5d$ and copper $3d$ orbitals. Radius of muffin tin (RMT) was selected to be $1.46, 1.48, 1.50, 2.00, 2.00, 1.94$ bohr for O, Li, Na, Ir, Sn, and Cu atoms and the basis size control parameter was $RK_{\text{max}} = 6$. Both structural relaxation and spectroscopic calculations were spin polarized and included spin orbit coupling (SOC).

1. Kitaev, A. Anyons in an exactly solved model and beyond. *Annals of Physics* **321**, 2–111 (2006). URL http://www.sciencedirect.com/science/article/pii/S0003491605002381.

2. Kitaev, A. Y. Fault-tolerant quantum computation by anyons. *Annals of Physics* **303**, 2–30 (2003). URL http://www.sciencedirect.com/science/article/pii/S0003491602000180.

3. Singh, Y. *et al.* Relevance of the Heisenberg-Kitaev Model for the Honeycomb Lattice Iridates A_2IrO_3. *Physical Review Letters* **108**, 127203 (2012). URL https://link.aps.org/doi/10.1103/PhysRevLett.108.127203.

4. Choi, S. K. *et al.* Spin Waves and Revised Crystal Structure of Honeycomb Iridate Na_2IrO_3. *Physical Review Letters* **108**, 127204 (2012). URL https://link.aps.org/doi/10.1103/PhysRevLett.108.127204.

5. Chaloupka, J., Jackeli, G. & Khaliullin, G. Zigzag Magnetic Order in the Iridium Oxide Na_2IrO_3. *Physical Review Letters* **110**, 097204 (2013). URL https://link.aps.org/doi/10.1103/PhysRevLett.110.097204.

6. Kimchi, I. & Vishwanath, A. Kitaev-Heisenberg models for iridates on the triangular, hyper-kagome, kagome, fcc, and pyrochlore lattices. *Physical Review B* **89**, 014414 (2014). URL https://link.aps.org/doi/10.1103/PhysRevB.89.014414.

7. Hwan Chun, S. *et al.* Direct evidence for dominant bond-directional interactions in a honeycomb lattice iridate Na_2IrO_3. *Nature Physics* **11**, 462–466 (2015). URL https://www.nature.com/articles/nphys3322.

8. Winter, S. M., Li, Y., Jeschke, H. O. & Valentì, R. Challenges in design of Kitaev materials: Magnetic interactions from competing energy scales. *Physical Review B* **93**, 214431 (2016). URL https://link.aps.org/doi/10.1103/PhysRevB.93.214431.

9. Mehlawat, K., Thamizhavel, A. & Singh, Y. Heat capacity evidence for proximity to the Kitaev quantum spin liquid in A_2IrO_3 (A =Na, Li). *Physical Review B* **95**, 144406 (2017). URL https://link.aps.org/doi/10.1103/PhysRevB.95.144406.

10. Kitagawa, K. *et al.* A spin-orbital-entangled quantum liquid on a honeycomb lattice. *Nature* **554**, 341–345 (2018). URL https://www.nature.com/articles/nature25482.

11. Slagle, K., Choi, W., Chern, L. E. & Kim, Y. B. Theory of a quantum spin liquid in the hydrogen-intercalated honeycomb iridate $H_3LiIr_2O_6$. *Physical Review B* **97**, 115159 (2018). URL https://link.aps.org/doi/10.1103/PhysRevB.97.115159.

12. Simutis, G. *et al.* Chemical and hydrostatic-pressure effects on the Kitaev honeycomb material Na_2IrO_3. *Physical Review B* **98**, 104421 (2018). URL https://link.aps.org/doi/10.1103/PhysRevB.98.104421.

13. Plumb, K. W. *et al.* α-$RuCl_3$: A spin-orbit assisted Mott insulator on a honeycomb lattice. *Physical Review B* **90**, 041112 (2014). URL https://link.aps.org/doi/10.1103/PhysRevB.90.041112.

14. Sears, J. A., Zhao, Y., Xu, Z., Lynn, J. W. & Kim, Y.-J. Phase diagram of α-$RuCl_3$ in an in-plane magnetic field. *Physical Review B* **95**, 180411 (2017). URL https://link.aps.org/doi/10.1103/PhysRevB.95.180411.

15. Takayama, T. *et al.* Hyperhoneycomb Iridate β-Li_2IrO_3 as a Platform for Kitaev Magnetism. *Physical Review Letters* **114**, 077202 (2015). URL https://link.aps.org/doi/10.1103/PhysRevLett.114.077202.

16. Veiga, L. S. I. *et al.* Pressure tuning of bond-directional exchange interactions and magnetic frustration in the hyperhoneycomb iridate β-Li_2IrO_3. *Physical Review B* **96**, 140402 (2017). URL https://link.aps.org/doi/10.1103/PhysRevB.96.140402.

17. Modic, K. A. *et al.* Realization of a three-dimensional spinâĂŞanisotropic harmonic honeycomb iridate. *Nature Communications* **5**, 4203 (2014). URL https://www.nature.com/articles/ncomms5203.

18. Abramchuk, M. *et al.* Cu_2IrO_3: A New Magnetically Frustrated Honeycomb Iridate. *Journal of the American Chemical Society* **139**, 15371–15376 (2017). URL https://doi.org/10.1021/jacs.7b06911.

19. Savary, L. & Balents, L. Quantum spin liquids: a review. *Reports on Progress in Physics* **80**, 016502 (2017). URL http://stacks.iop.org/0034-4885/80/i=1/a=016502.

20. Singh, Y. & Gegenwart, P. Antiferromagnetic Mott insulating state in single crystals of the honeycomb lattice material Na_2IrO_3. *Physical Review B* **82**, 064412 (2010). URL https://link.aps.org/doi/10.1103/PhysRevB.82.064412.

21. Chaloupka, J., Jackeli, G. & Khaliullin, G. Kitaev-Heisenberg Model on a Honeycomb Lattice: Possible Exotic Phases in Iridium Oxides A_2IrO_3. *Physical Review Letters* **105**, 027204 (2010). URL https://link.aps.org/doi/10.1103/PhysRevLett.105.027204.

22. Majumder, M. *et al.* Breakdown of Magnetic Order in the Pressurized Kitaev Iridate β-Li_2IrO_3. *Physical Review Letters* **120**, 237202 (2018). URL https://link.aps.org/doi/10.1103/PhysRevLett.120.237202.

23. Rau, J. G., Lee, E. K.-H. & Kee, H.-Y. Generic Spin Model for the Honeycomb Iridates beyond the Kitaev Limit. *Physical Review Letters* **112**, 077204 (2014). URL https://link.aps.org/doi/10.1103/PhysRevLett.112.077204.

24. Hu, K., Wang, F. & Feng, J. First-Principles Study of the Magnetic Structure of Na_2IrO_3. *Physical Review Letters* **115**, 167204 (2015). URL https://link.aps.org/doi/10.1103/PhysRevLett.115.167204.

25. Yaouanc, A. & Dalmas de Réotier, P. *Muon Spin Rotation, Relaxation, and Resonance: Applications to Condensed Matter*. International Series of Monographs on Physics (Oxford University Press, Oxford, New York, 2011).

26. Kalvius, G. M. *et al.* A μSR study of the ruthenium perovskites $ACu_3Ru_4O_{12}$ with A = Ca, Pr, Nd. *Journal of Physics: Conference Series* **551**, 012015 (2014). URL http://iopscience.iop.org/article/10.1088/1742-6596/551/1/012015.

27. Yamaji, Y., Nomura, Y., Kurita, M., Arita, R. & Imada, M. First-Principles Study of the Honeycomb-Lattice Iridates Na_2IrO_3 in the Presence of Strong Spin-Orbit Interaction and Electron Correlations. *Physical Review Letters* **113**, 107201 (2014). URL https://link.aps.org/doi/10.1103/PhysRevLett.113.107201.

28. Kim, B. J. *et al.* Novel $J_{\text{eff}} = 1/2$ Mott State Induced by Relativistic Spin-Orbit Coupling in Sr_2IrO_4. *Physical Review Letters* **101**, 076402 (2008). URL https://link.aps.org/doi/10.1103/PhysRevLett.101.076402.

29. Rehr, J. J. *et al.* Ab initio theory and calculations of X-ray spectra. *Comptes Rendus Physique* **10**, 548–559 (2009). URL http://www.sciencedirect.com/science/article/pii/S1631070508001084.

30. Abramchuk, M. *et al.* Crystal Chemistry and Phonon Heat Capacity in Quaternary Honeycomb Delafossites: $Cu[Li_{1/3}Sn_{2/3}]O_2$ and $Cu[Na_{1/3}Sn_{2/3}]O_2$. *Inorganic Chemistry* **57**, 12709–12717 (2018). URL https://doi.org/10.1021/acs.inorgchem.8b01866.

Acknowledgments We are grateful to Y. Ran for fruitful discussions. F.T. and M.A. acknowledge support from the National Science Foundation, Award No. DMR–1708929. MRCAT operations are supported by the Department of Energy and the MRCAT member institutions. This research used resources of the Advanced Photon Source, a U.S. Department of Energy (DOE) Office of Science User Facility operated for the DOE Office of Science by Argonne National Laboratory under Contract No. DE-AC02-06CH11357. Experiments at the ISIS Pulsed Neutron and Muon Source were supported by a beamtime allocation from the Science and Technology Facilities Council. O.I.L acknowledges financial support from the "Agence Nationale de la Recherche" in the framework of the "Investissements d'avenir" program with the reference "ANR–11–EQPX–0020" for EELS data obtained using GIF Quantum. W.L.-D.-H. and X.R. thank the HPC resources from GENCI-[TGCC/CINES/IDRIS] (Grant 2017-A0010907682). Work at APS was supported by the US Department of Energy (DOE), Office of Science, under Contract No. DE-AC02-06CH11357.

Author Contributions F.T. and M.J.G. designed the experiment and wrote the paper. E.M.K, A.B., S.P.C., and M.J.G. performed μSR experiments and analyzed data. C.U.S., J.L.M., G.F., and D.H. performed XANES experiments and analyzed data. W.L.-D.-H. and X.R. performed DFT calculations. G.S. analyzed data. M.A. and F.B. synthesized the material and performed X-ray refinements. O.I.L. and N.E.M. performed TEM and EELS experiments. All authors revised the manuscript.

Competing interests The authors declare no competing interests.

Supplementary information is available online.

Correspondence and requests for materials should be addressed to F.T. (email: fazel.tafti@bc.edu).